RSC Advances

PAPER

View Article Online
View Journal | View Issue

Cite this: *RSC Adv.*, 2024, **14**, 1501

Application of 3D printing technology for green synthesis of Fe_2O_3 using ABS/TPU/chlorella skeletons for methyl orange removal

Dingyong Liu,[acd] Hongjie Cai,[acd] Weiming Zhou,*[b] Dandan Lei,[acd] Changlin Cao,*[bcd] Xinshu Xia,[bcd] Liren Xiao,*[acd] Qingrong Qian[bcd] and Qinghua Chen[bcd]

Photocatalysis is widely acknowledged as an efficient and environmentally friendly method for treating dye-contaminated wastewater. However, the utilization of powdered photocatalysts presents significant challenges, including issues related to recyclability and the potential for secondary pollution. Herein, a novel technique based on 3D printing for the synthesizing of iron oxide (Fe_2O_3) involving chlorella was presented. Initially, chlorella powders were immobilized within acrylonitrile butadiene styrene (ABS) and thermoplastic polyurethane (TPU) substrate plastics using melt extrusion technology. Subsequently, these composite materials were transformed into ABS/TPU/chlorella skeletons (ATCh40), through fused deposition molding (FDM) technology. The integration of Fe_2O_3 onto the ATCh40 (ATCh40-Fe_2O_3) skeletons was accomplished by subjecting them to controlled heating in an oil bath. A comprehensive characterization of the synthesized materials confirms the successful growth of Fe_2O_3 on the surface of 3D skeletons. This strategy effectively addresses the immobilization challenges associated with powdered photocatalysts. In photocatalytic degradation experiments targeting methyl orange (MO), the ATCh40-Fe_2O_3 skeletons exhibited a remarkable MO removal rate of 91% within 240 min. Under conditions where the pH of MO solution was maintained at 3, and the ATCh40-Fe_2O_3 skeletons were subjected to a heat treatment in a 150 °C blast drying oven for 2 hours, the degradation rate of MO remained substantial, achieving 90% removal after 6 cycles. In contrast, when the same synthetic procedure was applied to ABS/TPU (AT) skeletons, the resulting product was identified as α-FeOOH. The MO removal rate by the AT-α-FeOOH skeletons was considerably lower, reaching only 49% after 240 min. This research provided a practical approach for the construction of photocatalytic devices through the use of 3D printing technology.

Received 20th October 2023
Accepted 7th December 2023

DOI: 10.1039/d3ra07143j

rsc.li/rsc-advances

1 Introduction

As society continues its progression, various industries are advancing by leaps and bounds. However, these advancements also bring forth the formidable challenge of effectively treating industrial wastewater. Among the most common forms of industrial wastewater, printing and dyeing wastewater stand out. Azo dyes, vital in various industrial applications like coloring plastics, rubber, and paints, are prevalent synthetic dyes. Methyl orange (MO) is one of the typical azo dyes; it is not only toxic and carcinogenic, but also poses severe health risks to humans. When substantial quantities of MO dye are introduced into an aqueous environment, it results in reduced levels of dissolved oxygen and sunlight penetration, consequently diminishing photosynthesis and causing great harm to the ecological environment.[1–3]

In recent years, a series of methods have been developed for addressing water pollution, including biodegradation, electrochemical, ion exchange, photocatalysis and adsorption.[4,5] Among these methods, photocatalysis stands out as one of the most convenient options, primarily due to its simplicity and relatively low cost, as it does not necessitate complex post-treatment procedures. Currently, widely utilized photocatalysts include ZnO,[6] TiO_2,[7] Bi_2O_3,[8] WO_3 (ref. 9) and g-C_3N_4.[10] Numerous other metal oxides have also been investigated as potential photocatalysts. Iron-based compounds have garnered significant interest among researchers in the field of photocatalysis due to their unique photosensitivity properties. For instance, Rizvi[11] *et al.* used fruit extract of *Hylocereus undatus* to

[a]*College of Chemistry and Materials Science, Fujian Normal University, Fuzhou 350117, China. E-mail: xlr1966@fjnu.edu.cn*

[b]*College of Environmental and Resource Sciences, College of Carbon Neutral Modern Industry, Fujian Normal University, Fuzhou 350117, China. E-mail: caochlin3@fjnu.edu.cn; zhouweiming721@126.com*

[c]*Engineering Research Center of Polymer Green Recycling of Ministry of Education, Fuzhou 350117, China*

[d]*Fujian Key Laboratory of Pollution Control & Resource Reuse, Fuzhou 350117, China*

synthesize iron oxide nanoparticles (IONPs), and investigated the effect of initial dye concentration, the amount of photocatalyst added, and the pH on photocatalytic degradation of metanil yellow and orange II dye. Similarly, Rodzi[12] *et al.* used chlorella extract to synthesize nano-iron oxide photocatalysts, achieving favorable outcomes in the degradation of crystal violet dye. Nathan[13] *et al.* employed a leaf extract from the mangrove plant *Rhizophora mucronata* to synthesize nano-iron oxide (Fe_2O_3-Nps) photocatalysts, the synthesized Fe_2O_3-Nps exhibited notable photodegradation efficiency with a reduction of 83% and 95% of phenol red and crystal violet under irradiation of sunlight and florescent light, respectively. Iron oxide (Fe_2O_3) and certain other ferrites can be synthesized using various techniques such as chemical coprecipitation, hydrothermal fabrication, and sacrificial template methods. However, the nanoscale structure of the synthesized powders often leads to issues such as agglomeration, inactivation and the potential for secondary pollution in aqueous solution. Additionally, their reusability has not been thoroughly addressed.

The application of 3D printing offers a promising solution to these challenges. Due to its capability for designing complex structures, facilitating batch manufacturing, and its ease of operation, 3D printing has found utility across various fields, including drug release,[14] wastewater treatment,[15] gas capture,[16] catalyst development.[17] In addressing the fixation of photocatalyst, Zhang *et al.*[6] employed a hydrothermal technique to immobilize nano-ZnO onto a $CaSiO_3$/ABS/TPU 3D skeleton for removing RhB, achieving a remarkable 90% removal ratio over six consecutive runs. Kennedy *et al.*[18] combined polylactic acid (PLA) with TiO_2 photocatalysts to produce a lattice using 3D printing, demonstrating an excellent photocatalytic efficacy. The 3D printed PLA-TiO_2 lattice effectively reduced microcystin (MC) cyanotoxin at a rapid pace. Nevertheless, the combination of plastic substrates with photocatalysis may accelerate plastic aging.[19] Polymer substrates are prone to generate microplastics during the aging process, which poses risks to both human health and the ecological environment. Consequently, exploring methods to further enhance the integration of photocatalyst with polymer substrates represents a worthwhile avenue for discussion.

In this work, an innovative approach for synthesizing Fe_2O_3 photocatalyst was invented. These photocatalyst composites were prepared through a combination of 3D printing and an oil bath heating method. As the polymer substrates, ABS and TPU were employed, while chlorella played a dual role by provided active sites and serving as a reactant in the synthesis process. The 3D-printed skeletons were created using filaments, which were obtained through the melt blending of ABS, TPU and chlorella. Subsequently, the photocatalysts, which were both reusable and effective, were generated through the oil bath heating process. The impact of various factors, including the photocatalyst type, Fe_2O_3 loading, and surface groups, on the photocatalytic properties of the samples were systematically investigated. Additionally, the relationships between the structure of the composites and its properties were analyzed in depth. Notably, when the same method was applied to ABS/TPU skeletons without the inclusion of chlorella, the resulting product was identified as α-FeOOH. It is essential to highlight that this synthesized α-FeOOH exhibited minimal degradation efficacy on MO dye. In this research, the photocatalyst was successfully embedded into the polymer substrate through a controlled heating process. After this heating treatment, the ATCh40 skeletons exhibited a significantly enhanced ability to immobilize the photocatalyst. This study offers a pragmatic approach for the construction of photocatalytic devices utilizing 3D printing technology and their application in the treatment of photodegradable wastewater. Synthetic Fe_2O_3 exhibited superior removal power for MO.

2 Experimental section

2.1 Materials

Commercial ABS (AG10AP) was purchased from Taiwan Chemical Fiber Co. Ltd. TPU 5377A was obtained from Bayer of Germany. Chlorella was obtained from Wu Di Green Qi Biological Engineering Co. Ltd. Ferrous sulphate heptahydrate ($FeSO_4 \cdot 7H_2O$) was supplied by Sinopharm Chemical Reagent Co. Ltd. Ethylene glycol $(CH_2OH)_2$ was obtained from Sinopharm Chemical Reagent Co. Ltd. Methyl orange (MO) was obtained from Aladdin Chemical Reagent Co. Ltd (Shanghai, China). All of the above materials were used without further purification.

2.2 Preparation of the ABS/TPU/chlorella skeletons and ABS/TPU skeletons

The ABS, TPU and chlorella underwent drying in a blast oven at temperatures of 80 °C, 80 °C and 110 °C, respectively, for a duration of 10 h. This drying process was carried out in accordance with the specified mass ratio of ABS, TPU, and chlorella, which was 70/30/40 for ATCh40 and 70/30/0 for AT, respectively. Subsequently, these materials were accurately weighed and uniformly mixed. This mixture was then subjected to a melt-blending process utilizing a twin-screw compounding extruder (MEDI-22/40, Guangzhou Putong Experimental Analysis Instrument Co. Ltd, China), followed by extrusion and pelletization. For ATCh40, the screw temperatures were set at 105 °C, 125 °C, 148 °C, 155 °C, 160 °C, 166 °C, 164 °C, 163 °C, 162 °C and 161 °C during the extrusion process. Meanwhile, the screw temperatures of AT were configured as 105 °C, 125 °C, 148 °C, 155 °C, 165 °C, 173 °C, 172 °C, 172 °C, 168 °C and 165 °C. The resulting pellets from the above granulator were subsequently utilizing a single-screw wire extruder (C type, Shenzhen Misida Technology Co. Ltd, China) to produce wires with a diameter of 1.75 ± 0.05 mm. The single-screw wire extruder for ATCh40 operated at temperatures of 112 °C, 154 °C, 160 °C, 152 °C, while for AT, temperatures of 116 °C, 166 °C, 177 °C, 168 °C were maintained. The screw speed employed was 25 rpm, resulting in production of ATCh40 and AT filament.

A 3D skeleton model was meticulously designed using a 3D CAD software. Subsequently, the printing parameters were configured using Cura software. The 3D printer employed for this purpose was the M2030 model (Shenzhen Soongon

Technology Co. Ltd, China). To ensure optimal printing quality, the 3D printer's settings were adjusted, including printing speed and printing temperature, in order to prepare ATCh40 and AT skeletons. The specific printing conditions on the 3D printer were as follows: a nozzle temperature of 200 °C, a base plate temperature of 90 °C, a print speed of 50 mm s^{-1}, utilization of 100% in-fill, a printed model layer thickness of 0.2 mm, and nozzles with a diameter of 0.40 mm. As a result of this printing process, the generated skeletons were denoted as ATCh40 and AT skeletons.

2.3 Synthesis of Fe_2O_3 and α-FeOOH nanospheres on the surface of 3D skeletons

The 0.4 M ATCh40-Fe_2O_3 skeletons and AT-α-FeOOH skeletons were synthesized *in situ* through a heating process conducted in an oil bath. The procedure commenced with the precise measurement of 17.8 g of $FeSO_4 \cdot 7H_2O$, followed by the addition of 128 ml of deionized water into the beaker. The beaker was sealed with plastic wrap, and the contents were stirred with a magnetic stirrer until complete dissolution was achieved. Subsequently, the solution was subjected to ultrasonication for a duration of 30 min.

Four ATCh40 skeletons and 32 ml of $(CH_2OH)_2$ were sequentially introduced into the above solution. The resultant mixture was once again sealed with plastic wrap, stirred and subjected to 30 min of ultrasonication. The solution, along with the incorporated skeletons, was transferred into 250 ml round bottom flask and subsequently placed in an oil bath set to a temperature of 80 °C. The mixture was stirred at a constant temperature for a period of 4 h. Following this, the reacted solution and skeletons were separated into two different beakers and allowed to cool naturally.

The reacted solution was centrifuged three times with anhydrous ethanol and centrifuged several times with deionized water until the upper layer appeared clear and colorless to remove impurities such as ethylene glycol in the solution, then left in blast drying oven at 60 °C. In parallel, the four reacted skeletons were washed with deionized water to eliminate ethylene glycol. Finally, the skeletons were subjected to drying in a blast drying oven at 60 °C until a constant weight was achieved, resulting in the production of 0.4 M ATCh40-Fe_2O_3 skeletons. By replacing ATCh40 skeletons with AT skeletons, the remaining synthetic steps remained identical, yielding AT-α-FeOOH skeletons (Fig. 1).

2.4 Characterization

The superficial micromorphology of the as-prepared samples was characterized using the JSM-7500F field emission scanning electron microscope (SEMJEOL, Japan). The micromorphology and element distribution of Fe_2O_3 on the surface of ATCh40 skeletons was further monitored *via* a FEI Tecnai G2 F30 transmission electron microscope (TEM, FEI, USA). To analyze the crystallographic properties, X-ray diffraction (XRD) analysis was conducted using a D8 Advance diffractometer (Bruker, Germany), employing a copper (Cu) target, 40 kV voltage, 40 mA current, with a testing range spanning 5–90° (2θ), and a testing rate of 6° min^{-1} (2θ). The surface chemical properties of the samples were recorded using Fourier-transform infrared spectroscopy (FTIR) (Thermo Fisher Scientific, USA). The chemical state and electronic structure of the samples were conducted using X-ray photoelectron spectroscopy (XPS) analysis (Thermo Scientific, USA). Vanquish Flex UHPLC Orbitrap Exploris 240 MS liquid chromatography-tandem mass spectroscopy (LC-MS) (Thermo Fisher Scientific, USA) was used to detect photocatalytic intermediates.

3 Results and discussion

3.1 Morphology studies

Fig. 2 showed the SEM images of the 3D printing skeletons. In Fig. 2a, the AT skeleton is depicted, showcasing a notably smoother surface compared to ATCh40 skeleton. Notably,

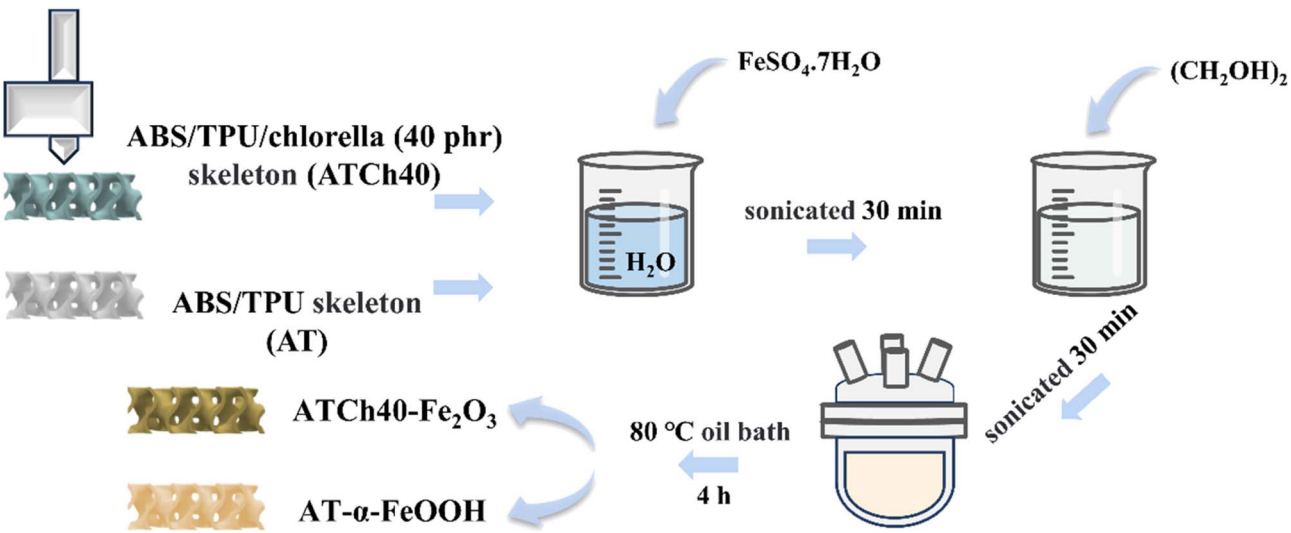

Fig. 1 Synthesis process of ATCh40-Fe_2O_3 skeleton and AT-α-FeOOH skeleton.

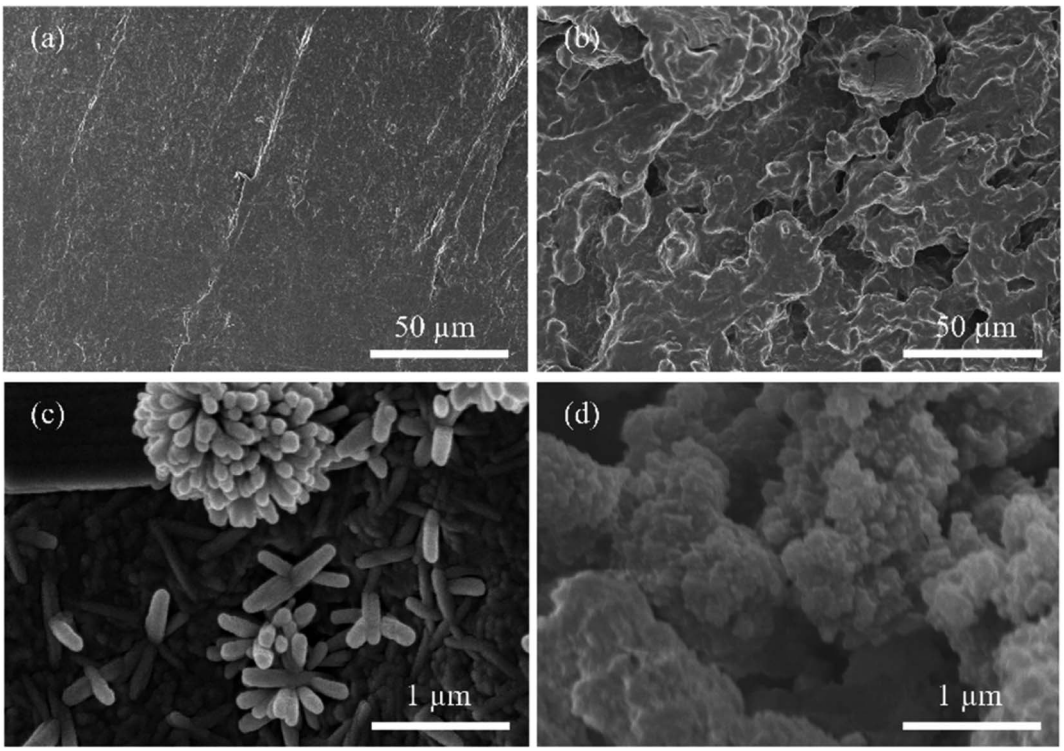

Fig. 2 SEM surface images of (a) AT skeleton, (b) ATCh40 skeleton, (c) AT-α-FeOOH skeleton, (d) ATCh40-Fe_2O_3 skeleton.

discernible scratches are observed on the AT skeleton's surface, which are attributed to the 3D printer nozzle during the printing process. It is important to the note that FDM 3D printers construct skeletons layer by layer through the use of nozzles. In Fig. 2b, the ATCh40 skeleton was illustrated, and its surface exhibits a comparatively rough texture. The ABS/TPU plastic substrates incorporate a substantial quantity of chlorella particles, some of which are wrapped within plastic substrates, visibly affecting the ATCh40 skeleton's surface. It is worth mentioning that 3D printing filaments exhibit high absorptive properties. ATCh40 filaments, unlike their AT counterparts, are less conducive to printing, resulting in a surface with fewer pronounced scratches. Fig. 2c offered a SEM image of the AT-α-FeOOH skeleton, where the synthesized α-FeOOH appears stick-shaped. On the surface of AT skeletons, α-FeOOH was dispersed uniformly, although some α-FeOOH clusters together, forming a "chrysanthemum-shaped" configuration. The AT skeleton's surface is characterized by a deficiency of active sites, potentially contributing to α-FeOOH agglomeration. It is also conceivable that the high surface energy of α-FeOOH triggers internal self-agglomeration,[20,21] Fig. 2d showed the SEM morphology of the ATCh40-Fe_2O_3 skeleton, demonstrating evident agglomeration of Fe_2O_3 particles on the surface of ATCh40 skeletons. Notably, the morphology of the synthesized Fe_2O_3 differs from α-FeOOH, exhibiting a "broccoli-shaped" structure. This discrepancy can potentially be attributed to chlorella secretions serving as reducing agents, promoting Fe_2O_3 particles formation during the oil bath process. Further agglomeration of Fe_2O_3 may result from a reduction in surface charge.[22,23] The morphology of individual Fe_2O_3 particles, as illustrated in Fig. 2d, is spherical, with a size of approximately 400 nm, consistent with the TEM result of Fig. 3a. In Fig. 3b, an HRTEM image showcased a single Fe_2O_3 particle, revealing lattice fringes with a spacing of approximately 0.25 nm. This lattice spacing corresponds to the (110) plane of Fe_2O_3, confirming the synthesis of Fe_2O_3 on the surface of ATCh40 skeletons.[24] Fig. 3c–f presented elemental mapping images of Fe_2O_3 synthesized on the surface of ATCh40 skeletons, encompassing the four elements: C, N, O, and Fe. The uniform distribution of C and N elements suggests Fe_2O_3 adsorbed trace amounts of chlorella secretions during the oil bath.

3.2 FTIR analysis

Fig. 4 illustrated the FTIR spectra of α-FeOOH, a mixture of ATCh40 skeleton and Fe_2O_3, Fe_2O_3, ATCh40 skeleton, all in powder form. Within these spectra, it is discernible that the absorption peak of ATCh40 skeleton, located near 3330 cm^{-1}, corresponding to the stretching vibration peak of the hydroxyl group. Interestingly, the vibration peaks of hydroxyl groups in α-FeOOH, ATCh40-Fe_2O_3 skeleton and Fe_2O_3 had shifted to 3400 cm^{-1}, which may be attributed to the alteration of some hydroxyl groups during the heating process in the oil bath. In the case of α-FeOOH grown on AT skeletons, two absorption vibration peaks are evident at 883 cm^{-1} and 794 cm^{-1}, primarily associate with the Fe–OH vibration in α-FeOOH. Additionally, the peak at 1637 cm^{-1} corresponds to the bending vibrations of H_2O molecule's H–O–H.[25] However, following the substitution of AT skeletons with ATCh40 skeletons, the surface loading of ATCh40 skeletons do not exhibit these two Fe–OH vibration

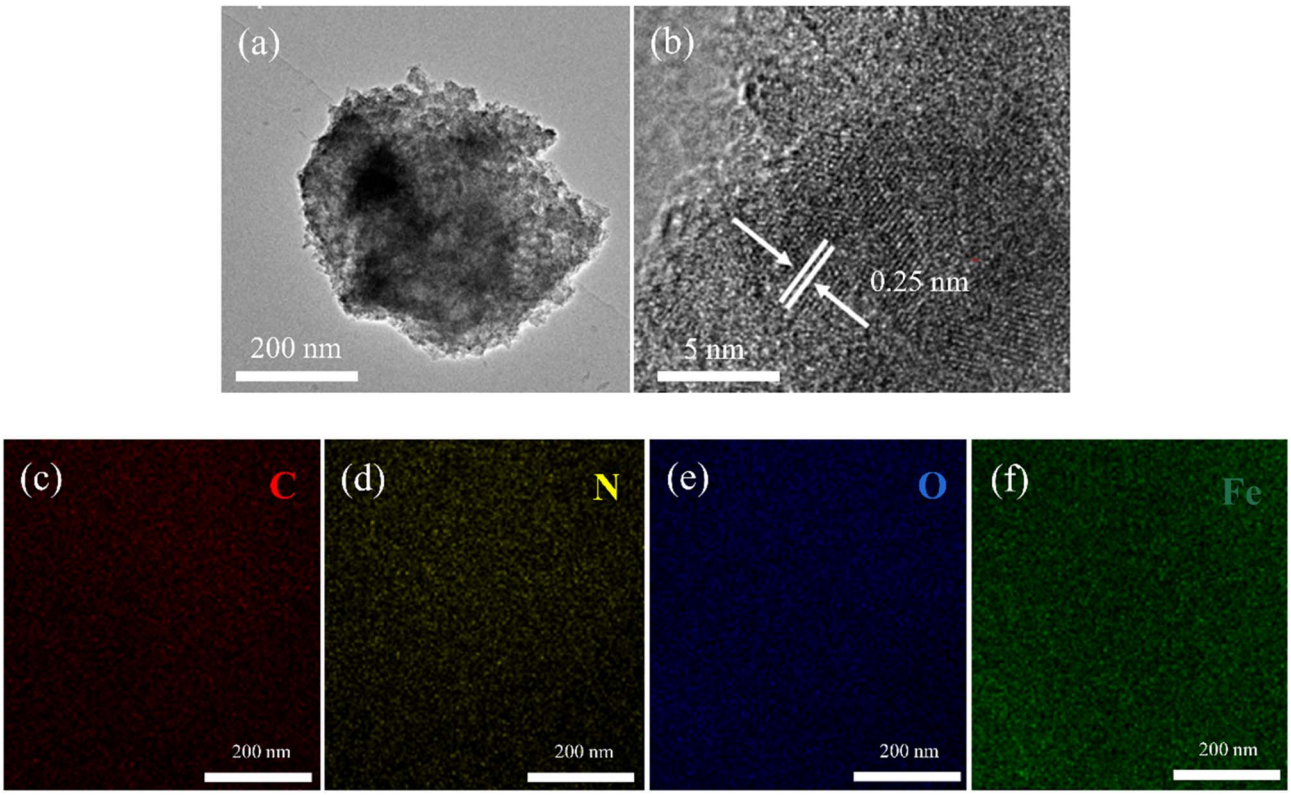

Fig. 3 TEM (a), HRTEM (b) images of Fe_2O_3 on the surface of ATCh40 skeletons, and elemental mapping images of C (c), N (d), O (e), Fe (f).

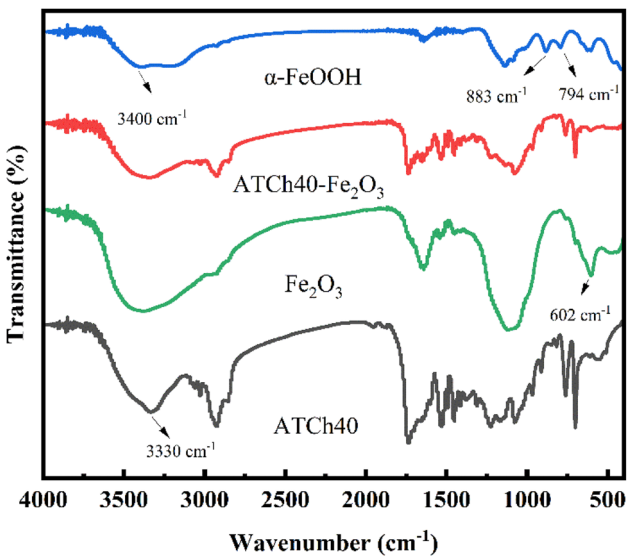

Fig. 4 FTIR of the α-FeOOH, ATCh40-Fe_2O_3 skeleton, Fe_2O_3 and ATCh40 skeleton.

peaks. This observation implies that after replacement of AT skeletons with ATCh40 skeletons, the resulting product is not α-FeOOH but another substance. Turning to the FTIR spectra of Fe_2O_3, a peak at 602 cm^{-1} represents the Fe–O vibration peak, while the peak at 1120 cm^{-1} may originate from chlorella secretions. The FTIR spectra of the substances synthesized on ATCh40 skeletons aligns closely with the characteristics of Fe_2O_3 as described in the literature.[26] Furthermore, CH_3 anti-symmetrical vibration peaks and CH_2 symmetrical vibration peaks, situating at 2930 cm^{-1} and 2850 cm^{-1}, respectively, corresponding to chlorella lipids and proteins. Peaks at 1230 cm^{-1} denote the stretching vibrations of the ester groups, whereas those at 1734 cm^{-1} are characteristic of TPU, reflecting C=O stretching vibration peaks.

3.3 XRD analysis

In Fig. 5, the XRD spectra of the various samples were presented. Notably, the diffraction peaks observed for α-FeOOH at 21.2°, 33.2°, 36.7°, 41.2°, 53.2° corresponds to the (110), (130), (111), (140), (221) crystal planes, respectively, of the rhombohedral crystal type $FeHO_2$ (JCPDS 00-029-0713). It is evident that the crystallinity of the Fe_2O_3 produced following the introduction of the ATCh40 skeletons is notably low. As illustrated, the peak at 35° corresponds to Fe_2O_3 (JCPDS 00-073-2234).[27] This reduced crystallinity of Fe_2O_3 synthesized on the ATCh40 skeletons can be attributed to the relatively low synthesis temperature, with the oil bath temperature maintained at only 80 °C. For the ATCh40-Fe_2O_3 samples (comprising a mixture of ATCh40 powders and Fe_2O_3 powders), an additional diffraction peak is evident at 20.6°. Importantly, samples of ATCh40, AT-α-FeOOH, and AT skeletons also exhibit a wide diffraction peak at 20.6°, indicating that these samples possess an amorphous nature.[6] The similarity in diffraction peaks between AT and AT-α-FeOOH skeletons suggest a relatively low loading of α-FeOOH

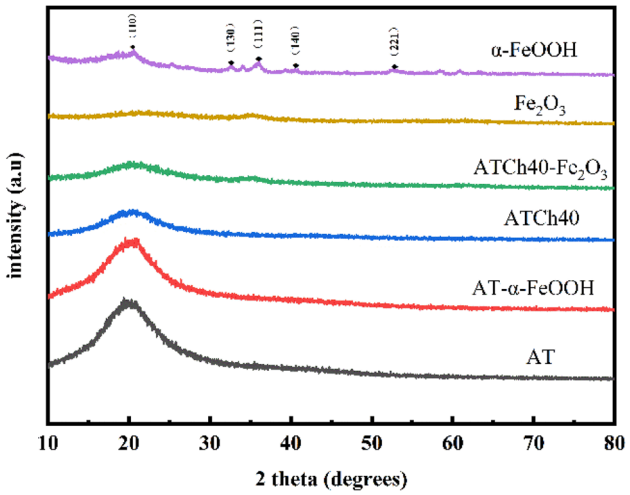

Fig. 5 XRD peaks of α-FeOOH, Fe_2O_3, ATCh40-Fe_2O_3 skeleton, ATCh40 skeleton, AT-α-FeOOH skeleton and AT skeleton.

on the AT skeletons. Intriguingly, after the introduction of chlorella, the diffraction peak of ATCh40 skeleton weakened at 20.6°, suggesting that chlorella may exert a shielding effect on the polymer.

3.4 XPS analysis

XPS analysis was employed to conduct an in-depth examination of the ATCh40 skeleton, ATCh40-Fe_2O_3 skeleton and Fe_2O_3, with the results displayed in Fig. 6a–c. In Fig. 6a, the C spectra of the ATCh40 and ATCh40-Fe_2O_3 skeletons are presented. The C element within ATCh40 skeletons exhibits three binding energies at 284.4 eV, 286.0 eV and 288.6 eV. These correspond to the C–C, C–H binding energies of ABS and chlorella within the skeleton, the C–O binding energy of chlorella and TPU, and the C═O binding energy of chlorella and TPU, respectively. The ATCh40-Fe_2O_3 peak reveals a narrowing of the binding energy domain at 284.4 eV after Fe_2O_3 was grown on ATCh40 skeletons.

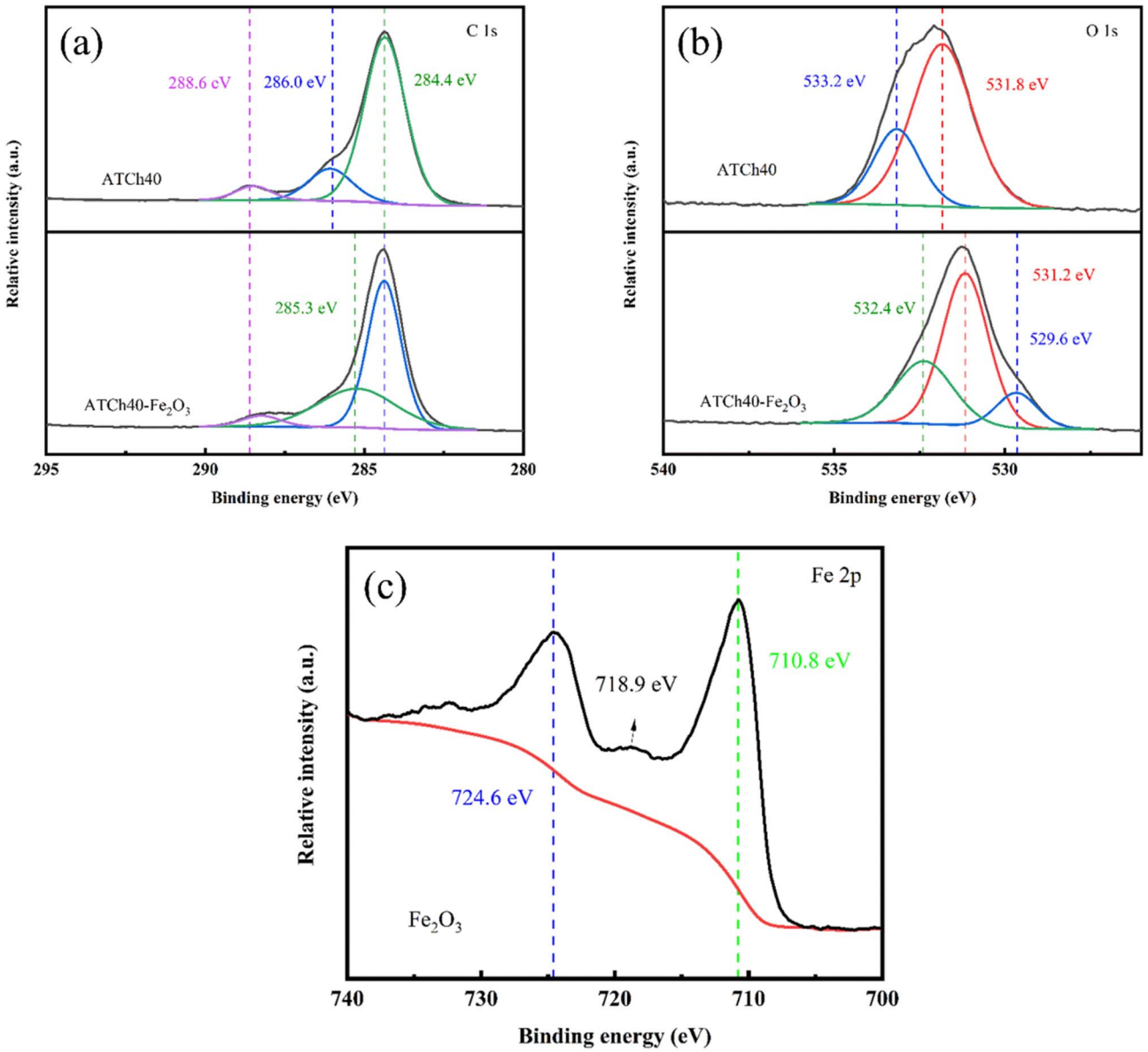

Fig. 6 XPS peaks of the (a) ATCh40 skeleton, (b) ATCh40-Fe_2O_3 skeleton and (c) Fe_2O_3.

Furthermore, the C–O binding energy shifted slightly lower from 286.0 eV, and the peak at 288.6 eV weakened. These observations suggest potential structural damage to chlorella during the oil bath process, involving the breakage of bonds and the destruction of functional groups.

Fig. 6b displayed the O spectra of the ATCh40 and ATCh40-Fe_2O_3 skeletons. In the ATCh40 skeletons, the O element exhibit two binding energies at 531.8 eV and 533.2 eV, corresponding to the C=O, C–O binding energies of chlorella within the skeletons, respectively. Following the growth of Fe_2O_3 on ATCh40 skeletons, the binding energies of ATCh40-Fe_2O_3 skeleton at 529.6 eV, 531.2 eV and 532.4 eV correspond to the lattice oxygen, vacancy oxygen, and organic oxygen binding energies of Fe_2O_3, respectively.

Fig. 6c presented the Fe spectra of the Fe_2O_3 grown on ATCh40 skeletons. The binding energy of the Fe_2O_3 at the peak of $Fe2p_{1/2}$ orbital was measured at 724.6 eV, while the binding energy at the peak of $Fe2p_{3/2}$ orbital was 710.8 eV, with the satellite peak likely at 718.9 eV. These values align precisely with the XPS peaks characteristic of Fe_2O_3.[28]

3.5 Photodegradation

In Fig. 7a, it is evident that the ATCh40 skeletons exhibit poor adsorption efficiency for methyl orange (MO) under dark condition. Within 240 min, the adsorption efficiency of ATCh40 skeleton towards MO is a mere 0.53%. This outcome can be attributed to the absence of functional groups capable of forming hydrogen bonds or electrostatic forces with MO. Additionally, the presence of SO_3^- in MO structures created mutual repulsion with adsorption functional groups on chlorella, further diminishing the adsorption capacity of ATCh40 skeleton towards MO. Even after loading photocatalysts, the dark adsorption efficiency of ATCh40-Fe_2O_3 skeletons for MO remains suboptimal, registering an adsorption efficiency of 31% within 240 min. However, the presence of Fe_2O_3 provides a wider mesoporous surface for ATCh40 skeletons. The surface properties of the synthesized Fe_2O_3, characterized by partial positive charges of iron ions, are conducive to the adsorption of anionic dye MO. Under the irradiation of xenon light source, the degradation rate of MO by ATCh40 skeletons reaches 30%, signifying a modest enhancement attributed to the

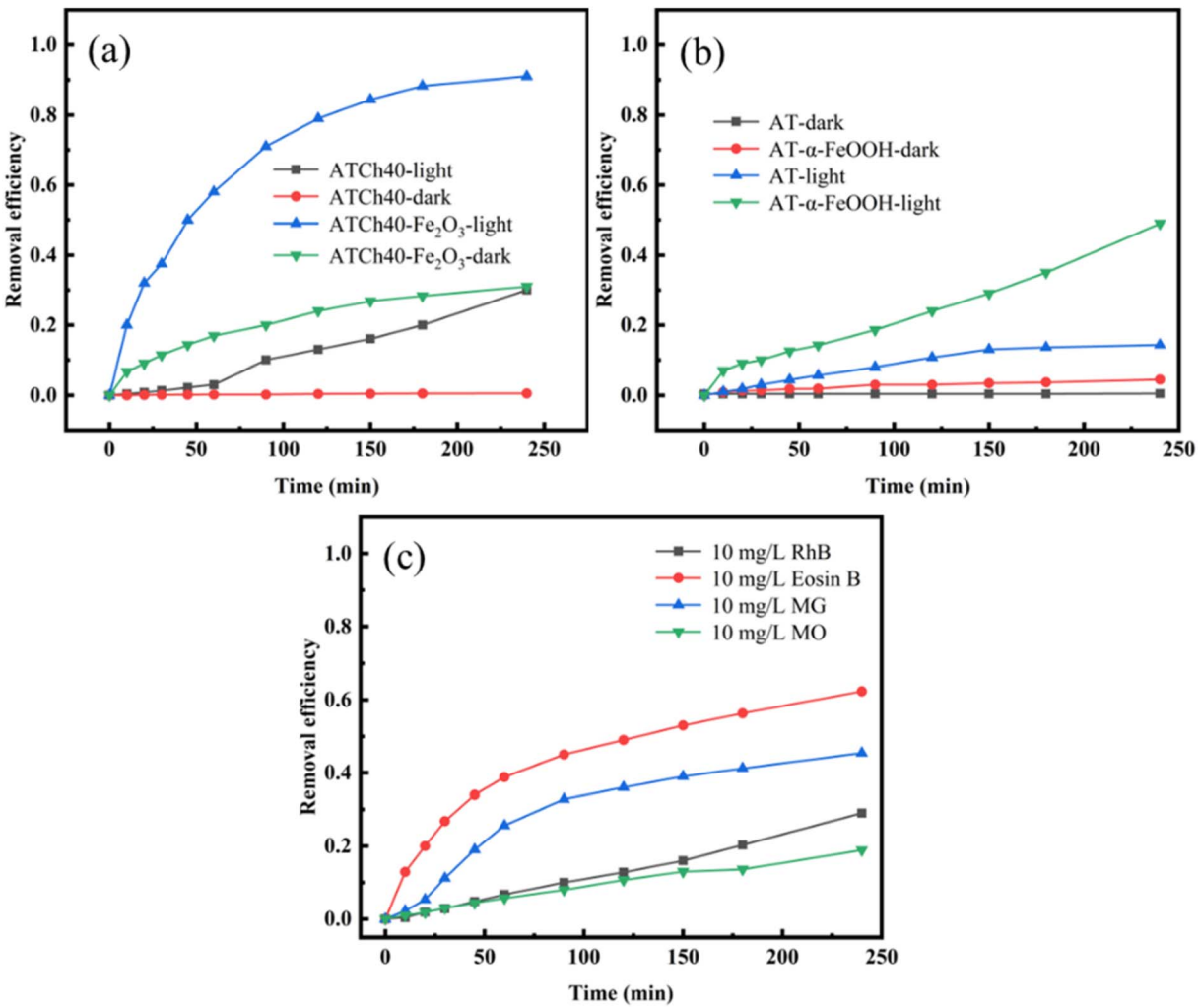

Fig. 7 (a) Degradation efficiency of MO (10 mg L^{-1}) by ATCh40 and ATCh40-Fe_2O_3 skeletons, (b) degradation efficiency of MO (10 mg L^{-1}) by AT and AT-α-FeOOH skeletons, (c) self-degradation curves of four dyes (10 mg L^{-1}).

photosensitization of chlorophyll in chlorella.[29] In contrast, when Fe_2O_3 was grown on the surface of ATCh40 skeletons, ATCh40-Fe_2O_3 skeletons exhibit a substantial enhancement in photodegradation and adsorption efficiency for MO under xenon lamp irradiation. Within 240 min, the degradation rate of MO reaches 91%. This observation underscores the remarkable photodegradation efficiency of the synthesized Fe_2O_3 photocatalyst under simulated sunlight, rather than solely under ultraviolet irradiation. Under the irradiation of xenon lamp, valence band electrons of Fe_2O_3 transferred to conduction band, generating a plethora of active free radicals. These radicals actively attacked the dye molecules, contributing to the enhanced photodegradation process. In Fig. 7b, it is evident that under dark conditions, the adsorption efficiency of AT and AT-α-FeOOH skeletons for MO is negligible. The AT skeletons lack active groups capable of adsorption, and the mesoporous surface generated by α-FeOOH are not as extensive as those produced by Fe_2O_3. Under the irradiation of xenon lamp, the degradation of MO by AT skeletons remains weak. AT skeletons neither adsorb MO nor exhibit a photocatalytic effect on MO. Instead, the degradation of MO primarily arises from its inherent self-degradation under light. In contrast, the degradation efficiency of MO by AT-α-FeOOH skeletons within 240 min reaches 49%. Notably, Fe_2O_3 possesses a smaller band gap compared to α-FeOOH, facilitating electron transmission and the generation of more active groups. In Fig. 7c, the self-degradation efficiency of four dyes under xenon lamp irradiation was depicted, with MO exhibiting the lowest self-degradation efficiency. This observation highlights the stability of MO properties and underscores the significance of studying MO in this experiment context. The molecular formula of MO features a large conjugated π–π structure comprised of benzene rings and a N=N bond, resulting in a low molecular system energy, which in turn enhances the stability of MO under simulated sunlight.

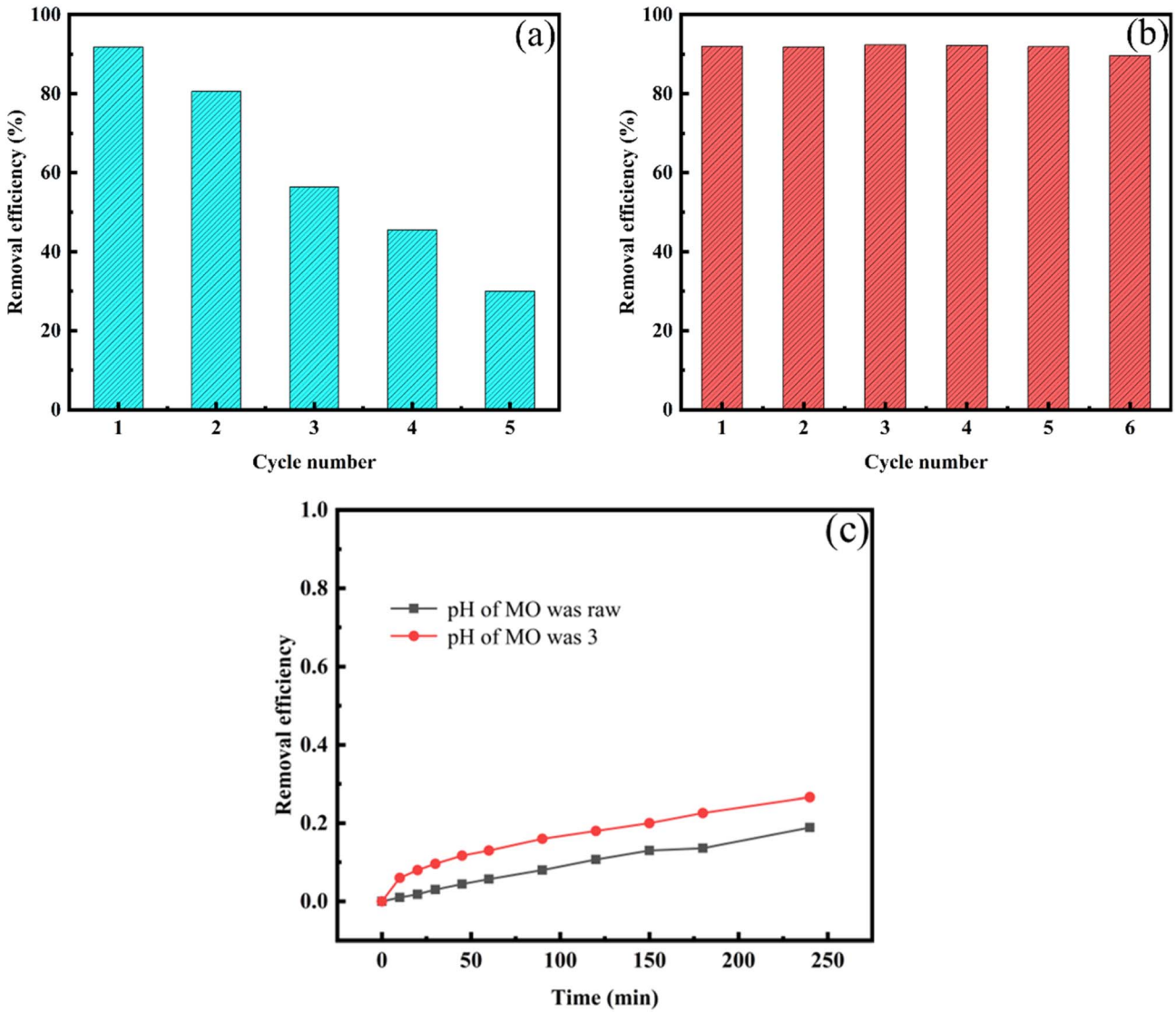

Fig. 8 Degradation efficiency of ATCh40-Fe_2O_3 skeletons after the reuse cycles: (a) pH of MO was raw; (b) pH of MO was 3; (c) self-degradation curves of MO (10 mg L^{-1}) under different pH.

3.6 Reusability experiments

The reusability of ATCh40-Fe_2O_3 skeletons for MO removal were thoroughly investigated. After undergoing five cycles, the photocatalytic-adsorption synergistic degradation efficiency of the ATCh40-Fe_2O_3 skeletons to MO over 240 min was depicted in Fig. 8a. The adsorbate was meticulously separated and desorbed using deionized water within an oscillating chamber for a duration of 12 h, maintained at a speed of 250 rpm. During this period, the water was refreshed every 2 h, followed by drying at 60 °C for 8 h in preparation for subsequent experiments. The outcomes of the five cycles were presented in Fig. 8a, revealing that after five cycles, the degradation rate of ATCh40-Fe_2O_3 skeletons to MO was only 30%. This indicated a decrease in cyclic removal efficiency, potentially attributable to incomplete desorption of the ATCh40-Fe_2O_3 skeletons, damage to adsorption sites, and partial separation of Fe_2O_3 from the skeleton surface during the experiment process. Consequently, several proposed schemes were considered to address these challenges. As illustrated in Fig. 8b, the ATCh40-Fe_2O_3 skeletons were subjected to a heat treatment in a 150 °C blast drying oven for 2 h to enhance the firm embedding of the catalysts within the ATCh40 skeletons. Additionally, the pH of MO was adjusted to 3. After implementing these conditions, cyclic degradation of MO by the ATCh40-Fe_2O_3 skeletons was performed once again. The results, depicted in Fig. 8b, showcases that after 6 cycles, the degradation efficiency of ATCh40-Fe_2O_3 skeletons to MO minimal reduction, with the degradation efficiency reaching an impressive 90%. The simple heating process significantly reduced the loss of photocatalysts during cycles. Under acidic conditions, MO formed a conjugated system featuring a para-quinone structure, resulting in a slight decrease in the stability of the dye structure. In Fig. 8c, when pH is 3, the stability of MO decreased slightly under xenon lamp irradiation. This suggestes that the improvement of cyclic performance in Fig. 8b was not due to the self-degradation of MO.

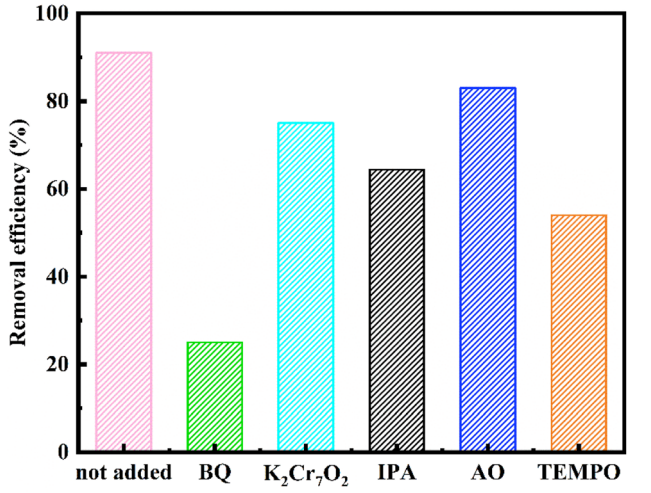

Fig. 9 Effects of different scavengers on the ATCh40-Fe_2O_3 skeletons degradation efficiency.

3.7 Mechanism

Active species trapping experiments were conducted to elucidate the effective free radicals involved in the reaction. In this experiment setup, various free radicals exhibited distinct affinities towards specific reagents. The removal rates of MO by ATCh40-Fe_2O_3 skeletons following the introduction of different trapping agents were illustrated in Fig. 9. Specifically, isopropanol (IPA) was employed to capture hydroxyl radicals ($OH^{\bullet}$), ammonium oxalate (AO) served as a scavenger for photogenerated holes (h^+), 1–4 benzoquinone (BQ) was utilized to trap superoxide radicals (O_2^-), and potassium dichromate ($K_2Cr_2O_7$) was chosen to capture photogenerated electrons (e^-),[30] as a control group, 2,2,6,6-tetramethyl-1-piperidinyloxy (TEMPO) was also used to inhibit free radicals.

The representative reaction equations for the degradation of MO were as follows:

$$\text{ATCh40-}Fe_2O_3 + h\nu \rightarrow e^-(CB) + h^+(VB) \quad (1)$$

$$e^-(CB) + O_2 \rightarrow O_2^- \quad (2)$$

$$Fe^{3+} + e^-(CB) \rightarrow Fe^{2+} \quad (3)$$

$$Fe^{2+} + O_2 \rightarrow Fe^{3+} + O_2^- \quad (4)$$

$$MO + O_2^- \rightarrow \text{degraded products} \quad (5)$$

$$h^+(VB) + H_2O \rightarrow OH^{\bullet} + H^+ \quad (6)$$

$$h^+(VB) + OH^- \rightarrow OH^{\bullet} \quad (7)$$

$$MO + OH^{\bullet} \rightarrow \text{degraded products} \quad (8)$$

The xenon light source emitted a substantial number of the incident photons. These photons were absorbed, leading to optical excitation, which facilitated the transfer of electrons from valence band to conduction band, resulting in the formation of electrons (e^-) and holes (h^+).[31] The photocatalytic degradation of MO necessitates the present of reactive oxygen species, namely $OH^{\bullet}$ and O_2^-. These species are generated through the reaction of H_2O and O_2 on the surface of ATCh40-Fe_2O_3 skeletons in the present of e^- and h^+, as shown in Fig. 9. Among these species. O_2^- played a pivotal role in the photocatalytic degradation of MO, while $OH^{\bullet}$, e^- and h^+ contributed partially to the promotion of the MO photocatalytic degradation. TEMPO could inhibit degradation, indicating that the reaction is a free radical reaction mechanism.[32,33] It's worth noting that the synthetic ferrite is trivalent and may have been doped with certain chlorella secretions, which can have played a vital role in inhibiting the recombination of e^- and h^+. Iron serves as the electron mediator for the photoexcited electrons within the conduction band, effectively facilitating the rapid separation of electron–hole pairs. The electrons in the conduction band can be effectively captured by Fe^{3+} ions, and the Fe^{2+} ions can react with O_2 to produce Fe^{3+} ions and O_2^-. Additionally, O_2^- can be generated directly from O_2. In summary, MO underwent various attack and binding

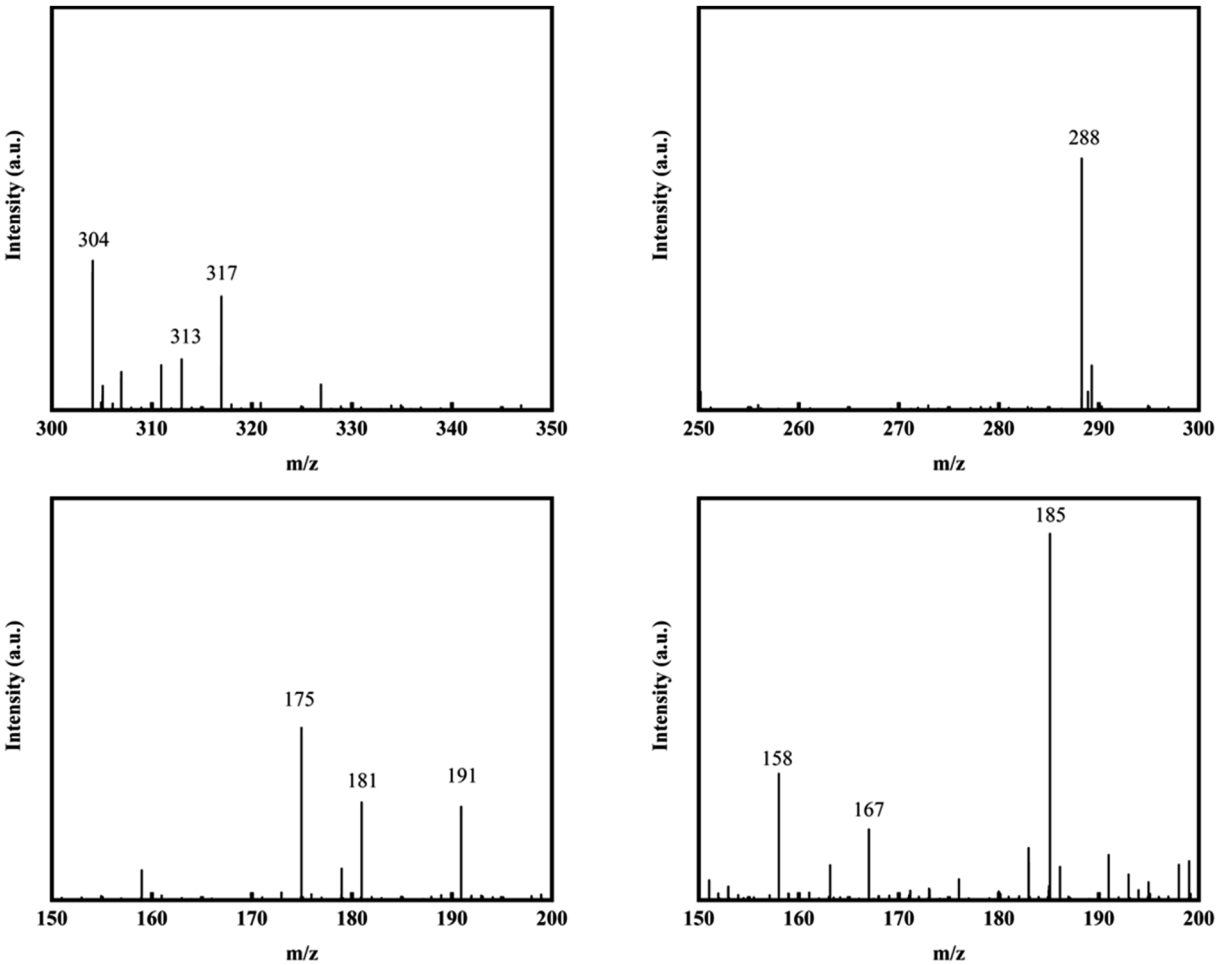

Fig. 10 Mass spectra of degradation products.

Table 1 Degradation intermediates of MO

RT (min)	*m*/*z*	Formula	Possible products
6.84	304	$C_{14}H_{14}N_3O_3S$	
9.56	288	$C_{13}H_{12}N_3O_4S$	
9.35	175	$C_6H_5O_4S$	
6.27	158	$C_6H_5O_3S$	

mechanisms involving $OH^{\bullet}$ and O_2^- species, resulting in the production of degradation products such as CO_2 and H_2O.

3.8 Analysis of degradation products

In this paper, LC-MS was used to explore the degradation products of MO in the photocatalytic degradation process. Fig. 10 showed the mass spectra of the four degradation products, the mass to charge ratio (*m*/*z*) and molecular structures of the four intermediate products were shown in Table 1. The new products appeared at RT 9.56, 9.35 and 6.27 min, respectively. When $m/z = 304$, the corresponding product is MO, the dimethylamino group of MO was attacked, causing the methyl group replaced by protons to form $C_{13}H_{12}N_3O_4S$. Subsequently, the methylamine group was removed, the benzene ring and –N=N– structure were replaced by hydroxyl group to form $C_6H_5O_4S$, which may be influenced by free radicals. The hydroxyl group was further removed to form $C_6H_5O_3S$.[34,35]

4 Conclusion

In this study, ATCh40-Fe_2O_3 composites were meticulously constructed by incorporating Fe_2O_3 with the ATCh40 skeletons

for photocatalytic degradation of MO. The innovative construction approach facilitated the immobilization of Fe_2O_3, effectively mitigating the environmental pollution typically associated with the use of standalone powdered photocatalysts. The presence of chlorella within the ATCh40 skeletons played a dual role, serving as attachment sites for Fe_2O_3 and actively participating in the formation of Fe_2O_3. Furthermore, it's noteworthy that the photocatalytic performance of ATCh40-Fe_2O_3 skeletons surpassed that AT-α-FeOOH skeletons. Following a more 4 h of photocatalytic degradation, the removal rate of MO achieved by the ATCh40-Fe_2O_3 skeletons reached an impressive 91%. To further optimize the reusability of ATCh40-Fe_2O_3 skeletons, a heat treatment at 150 °C for 2 h and pH adjustment to 3 led to a remarkable 90% MO removal even after 6 cycles.

This pioneering approach involves the integration of polymers, biomass, and photocatalysts for wastewater treatment, offering valuable insights and potential references for the development of novel water treatment materials in future research endeavors. Additionally, the study explored an innovative synthesis method leveraging chlorella to synthesize Fe_2O_3, marking a notable contribution to the field of materials synthesis.

Conflicts of interest

There are no conflicts to declare.

Acknowledgements

This work was financially supported by Public Welfare Scientific Research Project of Fujian Province (2022R1015001).

References

1 N. Ndlovu, I. Malatjie, C. Donga, *et al.*, Catalytic degradation of methyl orange using beta cyclodextrin modified polyvinylidene fluoride mixed matrix membranes imbedded with in-situ generated palladium nanoparticles, *J. Appl. Polym. Sci.*, 2023, **140**, 53270.
2 S. Z. Hu, Y. F. Deng, L. Li, *et al.*, Biomimetic Polylactic Acid Electrospun Fibers Grafted with Polyethyleneimine for Highly Efficient Methyl Orange and Cr(VI) Removal, *Langmuir*, 2023, **39**, 3770–3783.
3 E. Alzahrani, Zinc Oxide Nanopowders Prepared by the Sol-Gel Process for the Efficient Photodegradation of Methyl Orange, *Curr. Anal. Chem.*, 2016, **12**, 465–475.
4 C. R. Holkar, A. J. Jadhav, D. V. Pinjari, *et al.*, A critical review on textile wastewater treatments: Possible approaches, *J. Environ. Manage.*, 2016, **182**, 351–366.
5 L. Mouni, L. Belkhiri, J. C. Bollinger, *et al.*, Removal of Methylene Blue from aqueous solutions by adsorption on Kaolin: Kinetic and equilibrium studies, *Appl. Clay Sci.*, 2018, **153**, 38–45.
6 M. L. Zhang, X. S. Xia, C. L. Cao, *et al.*, A ZnO@ABS/TPU/$CaSiO_3$ 3D skeleton and its adsorption/photocatalysis properties for dye contaminant removal, *RSC Adv.*, 2020, **10**, 41272–41282.
7 K. Sathiyan, R. B. Ziv, O. Mendelson, *et al.*, Controllable synthesis of TiO_2 nanoparticles and their photocatalytic activity in dye degradation, *Mater. Res. Bull.*, 2020, **126**, 110842.
8 M. Saeed, A. U. Haq, M. Muneer, *et al.*, Synthesis and characterization of Bi_2O_3 and Ag-Bi_2O_3 and evaluation of their photocatalytic activities towards photodegradation of crystal violet dye, *Phys. Scr.*, 2021, **96**, 125707.
9 J. Q. Qiu, F. X. Xu, *et al.*, Hierarchical WO_3 microflowers with tailored oxygen vacancies for boosting photocatalytic dye degradation, *New J. Chem.*, 2021, **45**, 21074–21081.
10 R. T. Guo, J. Wang, Z. X. Bi, *et al.*, Recent advances and perspectives of g–C_3N_4–based materials for photocatalytic dyes degradation, *Chemosphere*, 2022, **295**, 133834.
11 M. Rizvi, N. Tiwari, A. Mishra, *et al.*, Kinetic and Computational Study of Degradation of Two Azo Dyes, Metanil Yellow and Orange II, by Iron Oxide Nanoparticles Synthesized Using Hylocereus undatus, *ACS Omega*, 2022, **7**, 31667–31681.
12 U. M. Rodzi, P. L. Kiew, M. K. Lam, *et al.*, A feasibility study on the green synthesis of iron oxide nanoparticles using Chlorella vulgaris extract for photocatalytic degradation of crystal violet, *IOP Conf. Ser.: Earth Environ. Sci.*, 2023, **1144**, 012004.
13 V. K. Nathan, P. Ammini and J. Vijayan, Photocatalytic degradation of synthetic dyes using iron (III) oxide nanoparticles (Fe_2O_3-Nps) synthesised using Rhizophora mucronata Lam, *IET Nanobiotechnol.*, 2019, **13**, 120–123.
14 J. Boetker, J. J. Water, J. Aho, *et al.*, Modifying release characteristics from 3D printed drug-eluting products, *Eur. J. Pharm. Sci.*, 2016, **90**, 47–52.
15 Z. L. Wang, Z. P. Han, X. Z. Liao, *et al.*, 3D printing polycaprolactone micro-nano copper scaffolds with a high antibacterial performance for potential sewage treatment, *High Perform. Polym.*, 2022, **34**, 44–53.
16 M. Xiao, M. Sarma, D. Nguyen, *et al.*, Efficient carbon capture using sub-textured polymer packing surfaces via 3D printing, *Chem. Eng. Sci.*, 2023, **267**, 118320.
17 C. Y. Chaparro-Garnica, E. Bailón-García, A. Davó-Quiñonero, *et al.*, High Performance Tunable Catalysts Prepared by Using 3D Printing, *Materials*, 2021, **14**, 5017.
18 A. J. Kennedy, A. D. McQueen, M. L. Ballentine, *et al.*, Degradation of microcystin algal toxin by 3D printable polymer immobilized photocatalytic TiO_2, *Chem. Eng. J.*, 2023, **455**, 140866.
19 Q. Y. Lee and H. Li, Photocatalytic Degradation of Plastic Waste: A Mini Review, *Micromachines*, 2021, **12**, 907.
20 S. L. Wan, Y. Li, S. Cheng, *et al.*, Cadmium removal by FeOOH nanoparticles accommodated in biochar: Effect of the negatively charged functional groups in host, *J. Hazard. Mater.*, 2022, **421**, 126807.
21 S. Lee, T. Lee and D. Kim, Adsorption of Hydrogen Sulfide from Gas Streams Using the Amorphous Composite of α-FeOOH and Activated Carbon Powder, *Ind. Eng. Chem. Res.*, 2017, **56**, 3116–3122.

22 A. Mohammed, I. A. Jassim, I. A. H ameed, *et al.*, Physical properties and antibacterial activity of green-iron oxide nanoparticles synthesize with chia seeds, *Chem. Data Collect.*, 2023, **44**, 101013.

23 Y. Zhuang, Y. Kong, Q. Z. Liu, *et al.*, Alcohol-assisted self-assembled 3D hierarchical iron (hydr)oxide nanostructures for water treatment, *CrystEngComm*, 2017, **19**, 5926–5933.

24 Y. Zheng, X. Zhang, J. Zhao, *et al.*, Assembled fabrication of α-Fe_2O_3/BiOCl heterojunctions with enhanced photocatalytic performance, *Appl. Surf. Sci.*, 2018, **430**, 585–594.

25 S. Kaufhold, K. Ufer, M. Hein, *et al.*, A combined IR and XRD study of natural well crystalline goethites (α-FeOOH), *Acta Geochim.*, 2022, **41**, 794–810.

26 S. Panikar, A. U. R. Nanthini, U. V. Rekha, *et al.*, Morphological, chemoprofile and soil analysis comparison of Corymbia citriodora (Hook.) K.D. Hill and L.A.S. Johnson along with the green synthesis of iron oxide nanoparticles, *J. King Saud Univ. Sci.*, 2022, **34**, 102081.

27 L. Shen, J. J. Wang, Z. F. Li, *et al.*, A high-efficiency Fe_2O_3@Microalgae composite for heavy metal removal from aqueous solution, *J. Water Process. Eng.*, 2020, **33**, 101026.

28 T. Yamashita and P. Hayes, Analysis of XPS spectra of Fe^{2+} and Fe^{3+} ions in oxide materials, *Appl. Surf. Sci.*, 2008, **254**, 2441–2449.

29 A. C. Bevilacqua, M. H. Köhler, B. A. Iglesias, *et al.*, Photophysical and photocatalytic properties of corrophyll and chlorophyll, *Comput. Mater. Sci.*, 2019, **158**, 228–234.

30 Z. Q. Li, W. Q. Li, H. Y. Shao, *et al.*, Water-Soluble Ag–Sn–S Nanocrystals Partially Coated with ZnS Shells for Photocatalytic Degradation of Organic Dyes, *ACS Appl. Nano Mater.*, 2023, **6**, 4417–4427.

31 M. R. Al-Mamun, M. Z. I. Rokon, M. A. Rahim, *et al.*, Enhanced photocatalytic activity of Cu and Ni-doped ZnO nanostructures: A comparative study of methyl orange dye degradation in aqueous solution, *Heliyon*, 2023, **9**, e16506.

32 Y. Chen, C. Chen, Y. H. Liu, *et al.*, Probing the effect of nitrate anion in CAN: An additional opportunity to reduce the catalyst loading for aerobic oxidations, *Chin. Chem. Lett.*, 2023, **34**, 108489.

33 Y. Y. Zhang, W. Li, Z. F. Hu, *et al.*, Mo@PANI-catalyzed oxidative deoximation reaction, *Chin. Chem. Lett.*, 2023, **35**, 108938.

34 P. Chen, Y. M. Liang, Y. F. Xu, *et al.*, Synchronous photosensitized degradation of methyl orange and methylene blue in water by visible-light irradiation, *J. Mol. Liq.*, 2021, **334**, 116159.

35 M. K. Renuka and V. Gayathri, UV/solar light induced photocatalytic degradation of phenols and dyes by Fe(PS-BBP)Cl_3, *J. Photochem. Photobiol., A*, 2018, **353**, 477–487.